The Astrophysical Journal Letters, 982:L46 (8pp), 2025 April 1 https://doi.org/10.3847/2041-8213/adbf0d

A New Approach to the Low-frequency Stochastic Gravitational-wave Background: Constraints from Quasars and the Astrometric Hellings–Downs Curve

Jeremy Darling
Center for Astrophysics and Space Astronomy, Department of Astrophysical and Planetary Sciences, University of Colorado, 389 UCB Boulder, CO 80309-0389, USA; jeremy.darling@colorado.edu
Received 2024 December 10; revised 2025 March 6; accepted 2025 March 6; published 2025 March 27

Abstract

We present new astrometric constraints on the stochastic gravitational-wave background and construct the first astrometric Hellings–Downs curve using quasar proper motions. From quadrupolar vector spherical harmonic fits to the Gaia proper motions of 1,108,858 quasars, we obtain a frequency-integrated upper limit on the gravitational-wave energy density, $h_{70}^2\Omega_{\rm GW} \leqslant 0.023$ (95% confidence limit), for frequencies between 11.2 nHz and 3.1×10^{-9} nHz ($1.33/t_0$). However, from the astrometric Hellings–Downs curve that describes the correlated proper motions between 2,104,609,881 quasar pairs as a function of their angular separation, we find a stronger constraint: a characteristic strain of $h_c \leqslant 2.7 \times 10^{-12}$ for $f_{\rm ref} = 1\ {\rm yr}^{-1}$ and $h_{70}^2\Omega_{\rm GW} \leqslant 0.0096$ at 95% confidence. We probe down to $\pm 0.005\ \mu{\rm as}^2\ {\rm yr}^{-2}$ in correlated power and obtain the lowest astrometric limit to date. This is also the first time that optical wavelength astrometry surpasses limits from radio-frequency interferometry. This astrometric analysis does not yet reach the sensitivity needed to detect the pulsar timing–based red gravitational-wave spectrum extrapolated to the quasar gravitational-wave sensitivity window, assuming that the turnover in the spectrum occurs at ∼1 nHz for massive black hole binaries. The limits presented here may exclude some exotic interpretations of the stochastic gravitational-wave background.

Unified Astronomy Thesaurus concepts: Gravitational waves (678); Gravitational wave astronomy (675); Astrometry (80); Quasars (1319); Proper motions (1295); Time domain astronomy (2109); Gaia (2360)

1. Introduction

Gravitational waves (GWs) have now been detected from binary black hole mergers at frequencies of 35–250 Hz by LIGO and as a gravitational-wave background via pulsar timing at 2–28 nHz (B. P. Abbott et al. 2016; G. Agazie et al. 2023). The gravitational waves seen in pulsar timing show a red spectrum that is consistent with a stochastic background rather than from single sources, but the provenance of the background remains unknown. The most likely source is massive black hole binaries, but other sources such as a cosmological primordial background are possible (A. Afzal et al. 2023). If the pulsar-timing signal arises from massive black hole binaries, then it will have a red spectrum with the characteristic dimensionless strain $h_c \propto f^{-2/3}$ but should turn over at some frequency, most likely $\lesssim$1 nHz (e.g., A. Sesana et al. 2004; M. Enoki & M. Nagashima 2007).

The steep spectrum presents an opportunity for astrometric gravitational-wave detection methods, which span lower frequencies but are typically less sensitive to strain than pulsar timing. Astrometric methods, whether they detect gravitational waves or produce an upper limit, can inform the interpretation of the pulsar-timing result, can resolve the ambiguity of the source of the signal, and could potentially inform our understanding of the eccentricity of massive black hole binaries and their environmental coupling by probing the low-frequency turnover in the gravitational-wave spectrum (e.g., S. Chen et al. 2017; L. Z. Kelley et al. 2017).

Pulsar-timing residuals measure the correlated radial motions induced by a stochastic gravitational-wave background that follow the Hellings–Downs (HD; R. W. Hellings & G. S. Downs 1983) curve, but gravitational waves produce correlated transverse angular motions as well (e.g., T. Pyne et al. 1996; C. R. Gwinn et al. 1997; L. G. Book & E. E. Flanagan 2011; J. Darling et al. 2018). Reductively, gravitational waves have a characteristic strain that manifests in pulsar timing as $h_c \sim \Delta f_s/f_s$ (f_s is the pulsar spin frequency), while angular deflections scale as $h_c \sim \delta\theta$. In practice, angular deflections are measured as proper motion μ over a timescale $\Delta t = 1/f$: $h_c \sim \delta\theta \sim \mu\Delta t \sim \mu/f$. Pulsar-timing or proper motion correlations (or cross correlations between the two) will therefore measure h_c^2, which is proportional to the gravitational-wave energy density (e.g., C. J. Moore et al. 2015).

Angular motions can be described using vector spherical harmonics (VSH; T. Pyne et al. 1996; C. R. Gwinn et al. 1997; L. G. Book & E. E. Flanagan 2011; J. Darling et al. 2018) or using generalized HD curves that include astrometric correlations (e.g., D. P. Mihaylov et al. 2018; L. O'Beirne & N. J. Cornish 2018; W. Qin et al. 2019; M. Çalışkan et al. 2024). VSH-based analyses of quasar proper motions have used very long baseline interferometry (VLBI) radio observations (C. R. Gwinn et al. 1997; O. Titov et al. 2011; J. Darling et al. 2018; S. Jaraba et al. 2023) and Gaia optical proper motions (Gaia Collaboration et al. 2016; S. Jaraba et al. 2023). No gravitational-wave signature has been detected to date via astrometry, and the best limits on the frequency-integrated energy density were obtained by S. Jaraba et al. (2023): $h_{70}^2\Omega_{\rm GW} \leqslant 0.087$ for frequencies in the range 4.2×10^{-18} Hz to 1.1×10^{-8} Hz based on Gaia proper motions (Gaia Collaboration et al. 2023) and $h_{70}^2\Omega_{\rm GW} \leqslant 0.024$ for 5.8×10^{-18} Hz to 1.4×10^{-9} Hz using the VLBI catalog

presented in A. E. Truebenbach & J. Darling (2017) and analyzed by J. Darling et al. (2018).

The dominant VSH mode produced by a stochastic gravitational-wave background is quadrupolar ($\ell = 2$). However, the Gaia quasar proper motions show VSH power at all scales, starting with E- and B-mode dipoles ($\ell \geqslant 1$; Gaia Collaboration et al. 2022 and this work). Aside from the E-mode dipole associated with the secular aberration drift caused primarily by the barycenter acceleration about the Galactic center (O. Titov et al. 2011; A. E. Truebenbach & J. Darling 2017; Gaia Collaboration et al. 2021), the significant VSH modes are most likely systematic to the Gaia observations and astrometric solutions (Gaia Collaboration et al. 2022). This issue with Gaia effectively sets a floor on the stochastic gravitational-wave background that can be detected using VSH fitting.

Here we present the first astrometric HD analysis of Gaia quasar proper motions and show that this technique does not seem to find a systematic floor, offering unprecedented astrometric sensitivity to gravitational waves. In Section 2, we review the astrometric signal expected from a stochastic gravitational-wave background. We describe the data sources and treatment in Section 3 and the astrometric methods in Section 4. Section 5 presents new limits on the background as measured by VSH and HD methods and examines the error budgets, systematic effects, and possibly intrinsic scatter in the astrometric correlations. Section 6 assesses the implications of these results in light of the pulsar-timing red spectrum and discusses future work.

We assume a flat ΛCDM cosmology with $H_0 = 70\,\mathrm{km\,s^{-1}\,Mpc^{-1}}$ and $\Omega_{M,0} = 0.3$. This is used to calculate look-back times, the corresponding gravitational-wave frequencies, and the cosmological gravitational-wave energy density. It is worth noting that the Hubble constant is a rate, which can be written as an angular rate for comparison to extragalactic proper motions: $H_0 = 15\,\mu\mathrm{as\,yr^{-1}}$.

2. Theory

The effect of gravitational waves on proper motions can be described in two mathematically equivalent ways: using VSH (F. Mignard & S. Klioner 2012) or angular correlation functions (e.g., D. P. Mihaylov et al. 2018; L. O'Beirne & N. J. Cornish 2018; W. Qin et al. 2019; M. Çalışkan et al. 2024). The VSH manifestation of gravitational-wave proper motions is in $\ell \geqslant 2$ modes with equal power in spheroidal "E" modes and toroidal "B" modes and is dominated by the quadrupole (T. Pyne et al. 1996; C. R. Gwinn et al. 1997; L. G. Book & E. E. Flanagan 2011; J. Darling et al. 2018). The total quadrupolar VSH power P_2 can be related to the cosmological gravitational-wave energy density Ω_{GW} as

$$\Omega_{\mathrm{GW}} = \frac{6}{5}\,\frac{1}{4\pi}\,\frac{P_2}{H_0^2} = 0.00042\,\frac{P_2}{(1\mu\mathrm{as\,yr^{-1}})^2}\,h_{70}^{-2}, \qquad (1)$$

where the factor of 6/5 corrects for the $\ell > 2$ modes (e.g., T. Pyne et al. 1996; C. R. Gwinn et al. 1997; L. G. Book & E. E. Flanagan 2011). The details of the VSH signal and fitting are well described elsewhere (e.g., F. Mignard & S. Klioner 2012; J. Darling et al. 2018), but we summarize our specific methods in Section 4.1.

Like the VSH, angular proper motion correlations will have two equal-power (and identical) terms. For the astrometric HD curves, the two terms correspond to proper motions along (∥) and across (⊥) the great circle connecting pairs of objects, which could be stars, pulsars, quasars, or other luminous sources (L. G. Book & E. E. Flanagan 2011; D. P. Mihaylov et al. 2018; L. O'Beirne & N. J. Cornish 2018; W. Qin et al. 2019; S. Golat & C. R. Contaldi 2022; M. Çalışkan et al. 2024; K. Inomata et al. 2024). The angular correlations of perpendicular proper motions $\Gamma_{\perp\perp}(\theta)$ and parallel proper motions $\Gamma_{\parallel\parallel}(\theta)$ depend on the separation θ between pairs of objects as

$$\Gamma_{\perp\perp}(\theta) = \Gamma_{\parallel\parallel}(\theta) = \frac{2\pi}{3}\left(1 - 7\sin^2\left(\frac{\theta}{2}\right) - 12\sin^2\left(\frac{\theta}{2}\right)\tan^2\left(\frac{\theta}{2}\right)\ln\left[\sin\left(\frac{\theta}{2}\right)\right]\right). \qquad (2)$$

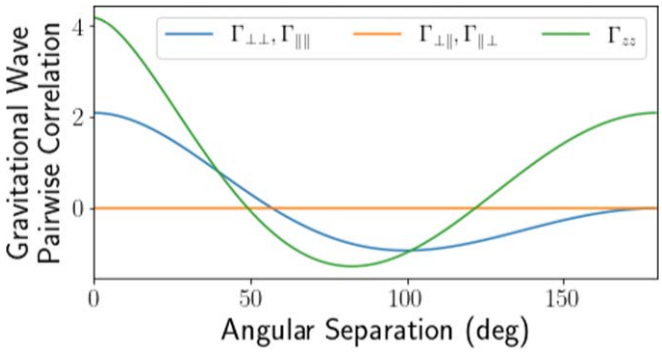

Figure 1. Generalized HD curves showing the predicted pairwise correlations of radial and angular motions produced by transverse traceless stochastic gravitational waves as a function of angular separation. The blue track shows the correlated angular motions along and perpendicular to the great circles connecting pairs of objects ($\Gamma_{\parallel\parallel}$ and $\Gamma_{\perp\perp}$, respectively). The orange track depicts the angular cross correlations, $\Gamma_{\perp\parallel}$ and $\Gamma_{\parallel\perp}$, which are expected to be null valued for all angular separations. The green line shows the canonical HD curve seen in pulsar timing that is caused by radial motions (Γ_{zz}).

This is the astrometric version of the radial HD curve used in pulsar timing (and depicted in Figure 1 as $\Gamma_{zz}(\theta)$ for reference). For a transverse traceless isotropic unpolarized gravitational-wave background, the cross-correlation terms vanish: $\Gamma_{\perp\parallel}(\theta) = \Gamma_{\parallel\perp}(\theta) = 0$ for all θ. This provides a powerful check on observational systematics because all four angular correlation functions can be calculated from 2D (vector) proper motions: the null-valued correlations provide a direct empirical measurement of any systematics present in the observations (see Section 4). Figure 1 shows the expected proper motion angular correlations.

The angular correlation between vector proper motions $\boldsymbol{\mu}$ is the observable quantity; it is the amplitude of this angular correlation signal that this analysis will seek. The average product of projected proper motions over all pairs of objects (n, m) with separation θ is

$$C_{ij}(\theta) \equiv \langle \mu_{n,i}\,\mu_{m,j}\rangle_\theta = f^3 I_{\mathrm{GW}}(f)\Gamma_{ij}(\theta), \qquad (3)$$

where i and $j \in \{\parallel, \perp\}$, and $I_{\mathrm{GW}}(f)$ is the gravitational-wave intensity, which is related to the characteristic strain as

$$h_c^2(f) = 16\pi f I_{\mathrm{GW}}(f) \qquad (4)$$

(M. Çalışkan et al. 2024). The cosmological energy density is related to the characteristic strain as

$$H_0^2\Omega_{\rm GW}(f) = \frac{2\pi^2}{3} f^2 h_c^2(f) \quad (5)$$

(C. J. Moore et al. 2015). Because $\Gamma_{ij}(\theta) = 0$ for $i \neq j$ for a transverse traceless unpolarized gravitational-wave background, the proper motion correlations provide a measurement of the characteristic strain for $i = j$:

$$h_c^2(f) = 16\pi \frac{C_{ii}(\theta)}{f^2\Gamma_{ii}(\theta)} \quad (6)$$

and the gravitational-wave energy density:

$$H_0^2\Omega_{\rm GW}(f) = \frac{32\pi^3}{3}\frac{C_{ii}(\theta)}{\Gamma_{ii}(\theta)}. \quad (7)$$

Expressing H_0 as an angular rate, we obtain the HD analog of Equation (1) that connects the observable quantity to the gravitational-wave energy density:

$$\Omega_{\rm GW}(f) = \frac{1.5}{\Gamma_{ii}(\theta)}\frac{C_{ii}(\theta)}{(1\,\mu{\rm as\ yr^{-1}})^2} h_{70}^{-2}. \quad (8)$$

Section 4.2 describes the process for projecting equatorial coordinate proper motion vectors parallel and perpendicular to great circles connecting pairs of objects in order to calculate $C_{\perp\perp}(\theta)$ and $C_{\parallel\parallel}(\theta)$.

3. Data

For this study, we select the Quaia quasar catalog, a compilation of Gaia-detected quasars in Gaia DR3 (Gaia Collaboration et al. 2023; K. Storey-Fisher et al. 2024). This sample has a large sky footprint, covering 73% of the sky nearly uniformly outside the $A_V > 0.5$ mag Galactic plane region, which makes this sample superior for all-sky measurements of proper motion fields. The catalog redshifts are not essential for this work because the proper motion signals are distance independent. We do, however, use the redshift distributions to estimate the lower bound on gravitational-wave frequency sensitivity (Section 4).

The Quaia samples include a 755,850-object catalog with Gaia $G < 20.0$ and a 1,295,502-object catalog with $G < 20.5$ (K. Storey-Fisher et al. 2024). We select Quaia quasars that have Gaia DR3 "5p" astrometric solutions: this reduces the samples to 688,367 quasars with $G < 20.0$ and 1,111,025 quasars with $G < 20.5$. In this work, we focus on the larger catalog because, while the magnitude cut does impact the Gaia astrometric solutions, there are sources in the larger catalog with low-uncertainty proper motion measurements. Given the median proper motion uncertainty of the sample, $\sim$200 μas yr^{-1}, we do not expect that any individual quasar will show significant real proper motion in the Gaia DR3. Those that do are spurious and are removed from the sample as described in Section 4.

The Gaia DR3 duration is 34 months, corresponding to a gravitational-wave frequency of $f_{\rm GW} = 11.2$ nHz. Because quasar proper motions are secular measurements, as opposed to pulsar-timing residuals, this is the upper limit on the frequency range spanned by the astrometry. The lower limit is set by the look-back time of the quasars and is of order 3×10^{-18} Hz (Section 4). The gravitational-wave frequencies probed by this method therefore span more than 10 orders of magnitude. Note that proper motions are quoted as the angular motion per year, but the actual frequency $1/f = 1$ yr is not directly sampled.

The DR3 quasar sample used for the Gaia astrometric solution, the third Gaia Celestial Reference Frame, shows correlations in proper motions on many angular scales, both toroidal and spheroidal (Gaia Collaboration et al. 2022). The secular aberration drift, the apparent E-mode dipole motion of quasars toward the Galactic center caused by the solar acceleration (O. Titov et al. 2011; A. E. Truebenbach & J. Darling 2017; Gaia Collaboration et al. 2021), is presumably the only physical signal in these correlations; all other VSH E modes and B modes are likely systematic to the observations and/or the astrometric solutions. It is noteworthy that a significant B-mode dipole exists in the Gaia DR3 quasars (Section 4.1), which indicates a rotating reference frame (or a rotating universe!).

The question at hand is whether the Gaia quasars' systematic global correlated proper motions prevent improved constraints on the stochastic gravitational-wave background. As demonstrated in Section 5, VSH fitting finds a nonphysical systematic floor in the quadrupolar power associated with gravitational waves. But do pairwise astrometric correlations show the same effect?

4. Astrometric Methods

In order to compare the two astrometric gravitational-wave detection methods, we present both VSH and astrometric HD fits to subsets of the Quaia $G < 20.5$ 5p catalog. The former shows significant dipole and quadrupole spheroidal and toroidal power, which motivates the astrometric HD analysis as a means to examine and perhaps overcome systematics in the Gaia DR3 proper motion solutions.

4.1. Vector Spherical Harmonics

While Gaia-based quasar proper motion samples that overlap the Quaia catalog have been used for VSH analysis focused on gravitational waves, such as the S. Jaraba et al. (2023) study using 773,471 quasars from Gaia DR3, the full Quaia catalog has not been analyzed. For completeness and as a comparison to the HD analysis, we present VSH dipole and quadrupole fitting here.

We employ the Quaia $G < 20.5$ catalog, excluding highly significant proper motions by imposing a signal-to-noise <4 cut in the proper motion amplitude. The resulting sample contains 1,108,858 quasars (99.8% of the 5p sample). In this sample, the redshift quartiles are $z = 1.07$, 1.51, and 2.01, corresponding to look-back times of 8.0, 9.3, and 10.3 Gyr and minimum GW frequencies of 4.0×10^{-18}, 3.4×10^{-18}, and 3.1×10^{-18} Hz. Following previous work, we use the 75th redshift percentile to set the lower bound on the effective integrated frequency (J. Darling et al. 2018; S. Jaraba et al. 2023). For the adopted cosmology, this corresponds to $1.33/t_0$.

We fit and remove the E- and B-mode dipoles (E1 and B1) from the proper motion data using a simple least-squares optimization. Simultaneous fits for the dipoles and quadrupoles are not significantly different from a sequential fit-and-subtract method with increasing ℓ, but we do the fitting of ℓ modes sequentially in order to match the dipole subtraction process used for the astrometric HD analysis below.

Table 1
Quaia 20.5 Dipole and Quadrupole VSH Fits

Parameter	Value (μas yr^{-1})	Parameter	Value (μas yr^{-1})
E Modes			
Dipole (Aberration Drift)		Quadrupole (GWs)	
s_{10}	−4.06(0.90)	s_{20}	−3.70(0.87)
s_{11}^{Re}	+0.67(0.66)	s_{21}^{Re}	+3.72(0.62)
s_{11}^{Im}	−10.22(0.63)	s_{21}^{Im}	+2.47(0.65)
$\sqrt{P_1^s}$	15.04(0.89)	s_{22}^{Re}	−2.76(0.68)
Amplitude	5.20(0.31)	s_{22}^{Im}	+2.34(0.68)
Z-score	13.1	$\sqrt{P_2^s}$	8.92(0.91)
B Modes			
Dipole (Rotation)		Quadrupole (GWs)	
t_{10}	−4.08(0.99)	t_{20}	+1.80(0.85)
t_{11}^{Re}	−5.03(0.66)	t_{21}^{Re}	+0.89(0.70)
t_{11}^{Im}	−2.66(0.60)	t_{21}^{Im}	+1.62(0.68)
$\sqrt{P_1^t}$	9.02(0.93)	t_{22}^{Re}	−1.31(0.63)
Amplitude	3.12(0.32)	t_{22}^{Im}	+0.91(0.63)
Z-score	8.2	$\sqrt{P_2^t}$	3.89(0.92)
Combined Modes			
$\sqrt{P_1}$	17.54(0.90)	$\sqrt{P_2}$	9.74(0.91)
Z-score	15.5	Z-score	8.5

Note. Proper motions are simultaneously fit to electric and magnetic dipole vector fields, the dipoles are subtracted from the proper motion data, and then quadrupoles are simultaneously fit to the residual. The VSH coefficients, power, and amplitudes are defined in the Appendix. Parenthetical quantities indicate 1σ uncertainties. The Z-score statistic, defined in F. Mignard & S. Klioner (2012), is unitless.

The best-fit E-mode dipole shows a streaming motion of 5.20 ± 0.31 μas yr^{-1} (Table 1). The E1 apex lies at the equatorial coordinates 273.°8(3.°7) −15.°8(3.°5), somewhat offset from the expected direction of the secular aberration drift, which is toward the Galactic center. The aberration drift is the result of the solar system barycenter acceleration toward the Galactic center as the Sun orbits the Galaxy. The changing aberration of distant quasars causes them to appear to move toward the Galactic center (O. Titov et al. 2011; A. E. Truebenbach & J. Darling 2017; Gaia Collaboration et al. 2021).

The best-fit B-mode dipole has a significant amplitude of 3.12 ± 0.32 μas yr^{-1} that can be thought of as the angular velocity of rotation, either of the observer or the reference frame (the Universe at large). The B1 apex[1] lies at 27.°9(6.°2) −26.°9(6.°2), equatorial. This is unlikely to be physical under the assumption that the Gaia reference frame shows rotation. Regardless, we subtract both of the highly significant dipole signals from the Quaia proper motions before fitting quadrupoles to the proper motion vector field.

The two quadrupolar VSH modes have five coefficients each, and their sum in quadrature is (modulo factors of 2) the power in each mode. The Appendix details the functional forms fit to the proper motion data, the computation of mode power, and the expressions for dipole amplitude and direction. One can employ more sophisticated VSH fitting that de-weights

[1] By "apex," we mean the center of an anticyclonic flow in the southern hemisphere, which follows the right-hand rule.

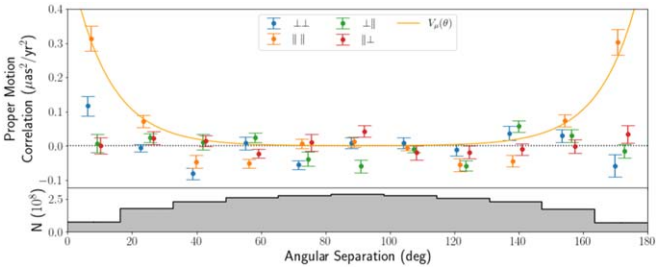

Figure 2. Proper motion power in the four correlations (Equations (16)–(19)) vs. the angular separation of quasar pairs for a sample of 67,917 quasars. These were selected based on a proper motion amplitude uncertainty <150 μas yr^{-1} and show a systematic in the $C_{\parallel\parallel}$ correlation (Equation (17)). The orange line shows the best fit of this systematic, described by $V_\mu(\theta)$ in Equation (9), a modified version of the quasar proper motion uncertainty correlation found in Gaia eDR3 by L. Lindegren et al. (2021). The points are laterally offset a few degrees from the center of each angular separation bin for clarity. The lower histogram shows the distribution of quasar pairs, scaled by 10^8.

significant outlier data or that employs Markov Chain Monte Carlo methods as described in J. Darling et al. (2018), but the differences in outcomes are negligible given the size of the sample and the significance of the power in the dipole and quadrupole modes.

4.2. Astrometric Hellings–Downs Correlations

For this treatment, we select all quasars with proper motion amplitude less than 100 μas yr^{-1}, which reduces the sample to 64,879 quasars. The reason for the down-select to this best-measured subset is that the error-weighted two-point proper motion correlations described below show diminishing uncertainty improvement as the proper motion cut is increased, reaching a minimum around a cut of 100 μas yr^{-1}. For example, selection of proper motion amplitude <110 μas yr^{-1} produces a sample of 76,588 quasars but ∼9% larger median uncertainties in the astrometric HD curve.

We also explored selection based on proper motion amplitude uncertainty. Choosing uncertainties <150 μas yr^{-1} produces a similar-sized sample of 67,917 quasars, but this sample shows a notable systematic correlation resembling the proper motion uncertainty correlation found by L. Lindegren et al. (2021) in Gaia eDR3 (early DR3) quasars. At small and large angular separations, proper motions parallel to the great circles connecting pairs of quasars are significantly correlated, as demonstrated in Figure 2 (the calculation and meaning of the proper motion correlations are described below in this subsection). L. Lindegren et al. (2021) fit the small-separation systematic using an exponential with characteristic scale of 12°. We fit the systematic plotted in Figure 2 using exponentials at high and low angular separations using the same angular scale:

$$V_\mu(\theta) = A_{\rm sys}(e^{-\theta/12^\circ} + e^{(\theta-180^\circ)/12^\circ}), \quad (9)$$

where $A_{\rm sys}$ is the amplitude of the correlation. An additional constant offset was also fit but was consistent with zero and is therefore omitted from Equation (9). We obtain $A_{\rm sys} = 0.56 \pm 0.11$ μas^2 yr^{-2}, which is significant and presents a prohibitive obstacle to measuring the astrometric HD signal using this uncertainty-based selection method.

For the 64,879-quasar proper motion–selected sample, the number of unique pairs used for the astrometric HD calculation is 2,104,609,881. In this sample, the redshift quartiles are $z = 0.93$, 1.41, and 1.92, corresponding to look-back times of

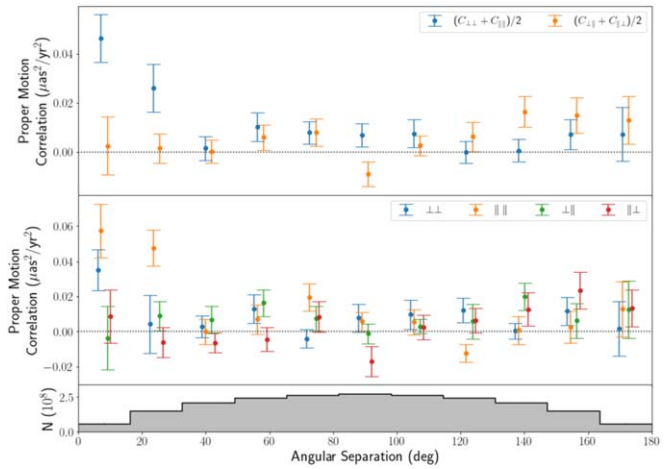

Figure 3. Angular correlations of quasar proper motions show significant excess power when the E- and B-mode dipoles are not removed. Top: aligned parallel and perpendicular modes (blue) and mixed modes (orange) vs. the angular separation of quasar pairs for 64,879 quasars selected for proper motion amplitude <100 μas yr^{-1}. The points are laterally offset from the center of each angular separation bin for clarity. Middle: all four individual proper motion correlation combinations. Bottom: the distribution of quasar pairs, scaled by 10^8.

7.4, 9.0, and 10.1 Gyr and minimum GW frequencies of 4.3×10^{-18}, 3.5×10^{-18}, and 3.1×10^{-18} Hz. We fit and subtract the E- and B-mode proper motion dipoles (using VSH fitting) from the proper motions of this specific sample in order to isolate higher modes. When these are not removed from the proper motion catalog, significant excess power remains and the astrometric HD signal cannot be recovered or constrained. Figure 3 shows the impact of failing to remove the dipoles before calculating the proper motion angular correlations. Most notably, the aligned proper motion correlations show a significant 3.9σ positive error-weighted mean.

In order to obtain the proper motion projections used in the astrometric HD calculation, we need to find the great-circle directions connecting an arbitrary pair of quasars. First, we construct the radial unit vector corresponding to the equatorial coordinates (α_n, δ_n) of object n:

$$\hat{\boldsymbol{n}} = \begin{pmatrix} \cos\alpha_n \cos\delta_n \\ \sin\alpha_n \cos\delta_n \\ \sin\delta_n \end{pmatrix}. \tag{10}$$

For a second object in direction $\hat{\boldsymbol{m}}$, the angular separation θ between $\hat{\boldsymbol{n}}$ and $\hat{\boldsymbol{m}}$ is

$$\cos\theta = \hat{\boldsymbol{n}} \cdot \hat{\boldsymbol{m}}. \tag{11}$$

This angle θ is the abscissa in the HD curve (Equation (2) and Figure 1).

The 3D proper motion vector is the time derivative of the position unit vector:

$$\boldsymbol{\mu}_n = \begin{pmatrix} -\mu_{n,\alpha} \sin\alpha_n \cos\delta_n - \mu_{n,\delta} \cos\alpha_n \sin\delta_n \\ \mu_{n,\alpha} \cos\alpha_n \cos\delta_n - \mu_{n,\delta} \sin\alpha_n \sin\delta_n \\ \mu_{n,\delta} \cos\delta_n \end{pmatrix}. \tag{12}$$

Note that $\boldsymbol{\mu}_n$ lies on the celestial sphere, as required: $\hat{\boldsymbol{n}} \cdot \boldsymbol{\mu}_n = 0$. Also, all of the time derivatives are with respect to the present cosmic time, t_0, and we neglect the minuscule radial change in the quasar position due to peculiar motions, the secular redshift drift (J. Darling 2012; M. Moresco et al. 2022), and the radial component of gravitational waves. The latter can be cross-correlated with angular motions and will likely be a powerful tool for combined pulsar timing and astrometry (e.g., D. P. Mihaylov et al. 2018).

The proper motion of each quasar in direction $\hat{\boldsymbol{n}}$ will have a component along and perpendicular to the great-circle path to the quasar at $\hat{\boldsymbol{m}}$, and the same will be true for the proper motion of $\hat{\boldsymbol{m}}$ with respect to the path to $\hat{\boldsymbol{n}}$. The unit vector $\hat{\boldsymbol{e}}_\perp$ perpendicular to the great circle connecting $\hat{\boldsymbol{n}}$ to $\hat{\boldsymbol{m}}$ is the same for n and m, but the unit vectors along the great circle are not the same and will be designated $\hat{\boldsymbol{e}}_{\parallel,n}$ and $\hat{\boldsymbol{e}}_{\parallel,m}$. We construct these unit vectors perpendicular and parallel to the great circle that connects $\hat{\boldsymbol{n}}$ to $\hat{\boldsymbol{m}}$:

$$\hat{\boldsymbol{e}}_\perp = \frac{\hat{\boldsymbol{n}} \times \hat{\boldsymbol{m}}}{\sqrt{1 - (\hat{\boldsymbol{n}} \cdot \hat{\boldsymbol{m}})^2}} \tag{13}$$

$$\hat{\boldsymbol{e}}_{\parallel,n} = \hat{\boldsymbol{e}}_\perp \times \hat{\boldsymbol{n}} \tag{14}$$

$$\hat{\boldsymbol{e}}_{\parallel,m} = \hat{\boldsymbol{e}}_\perp \times \hat{\boldsymbol{m}} \tag{15}$$

(D. P. Mihaylov et al. 2018; M. Çalışkan et al. 2024).

We calculate four proper motion correlations between pairs of quasars, corresponding to all combinations of motion perpendicular to and parallel to the great circle connecting each pair. The two correlations that are sensitive to a stochastic gravitational-wave background are

$$C_{\perp\perp}(\theta) \equiv \langle \mu_{n,\perp}\, \mu_{m,\perp} \rangle_\theta = \langle (\boldsymbol{\mu}_n \cdot \hat{\boldsymbol{e}}_\perp)(\boldsymbol{\mu}_m \cdot \hat{\boldsymbol{e}}_\perp) \rangle_\theta \tag{16}$$

$$C_{\parallel\parallel}(\theta) \equiv \langle \mu_{n,\parallel}\, \mu_{m,\parallel} \rangle_\theta = \langle (\boldsymbol{\mu}_n \cdot \hat{\boldsymbol{e}}_{\parallel,n})(\boldsymbol{\mu}_m \cdot \hat{\boldsymbol{e}}_{\parallel,m}) \rangle_\theta. \tag{17}$$

The angle brackets indicate an average of all pairs at a given θ (in practice, one uses a range $\Delta\theta$ centered at θ). The two cross-projection correlations are

$$C_{\perp\parallel}(\theta) \equiv \langle \mu_{n,\perp} \mu_{m,\parallel} \rangle_\theta = \langle (\boldsymbol{\mu}_n \cdot \hat{\boldsymbol{e}}_\perp)(\boldsymbol{\mu}_m \cdot \hat{\boldsymbol{e}}_{\parallel,m}) \rangle_\theta \tag{18}$$

$$C_{\parallel\perp}(\theta) \equiv \langle \mu_{n,\parallel} \mu_{m,\perp} \rangle_\theta = \langle (\boldsymbol{\mu}_n \cdot \hat{\boldsymbol{e}}_{\parallel,n})(\boldsymbol{\mu}_m \cdot \hat{\boldsymbol{e}}_\perp) \rangle_\theta. \tag{19}$$

These should be zero for unpolarized transverse traceless gravitational waves (e.g., W. Qin et al. 2019). These cross-term correlations provide a powerful check on systematics and can be compared in a one-to-one fashion to the aligned-projection correlations. Absent systematic structure, the cross terms also assess the statistical errors: comparison of the scatter to the uncertainties can be used to assess the appropriateness of the uncertainty estimates and the independence of the measurements.

To calculate the four correlations, we project the proper motions for each quasar pair parallel and perpendicular to each pair's great circle, form the product of these projections and their cross terms, bin in angular separation θ, and compute an error-weighted mean of each angular separation bin. To estimate the uncertainties in each bin, we bootstrap the error-weighted mean based on resampling quasar pairs. The bootstrap reveals no bias in the error-weighted mean. The number of angular separation bins is chosen to maximize signal-to-noise while adequately sampling the astrometric HD curve. We deliberately use an odd number of bins in order to sample any signal at $\theta = 90^\circ$, either in the aligned or cross terms.

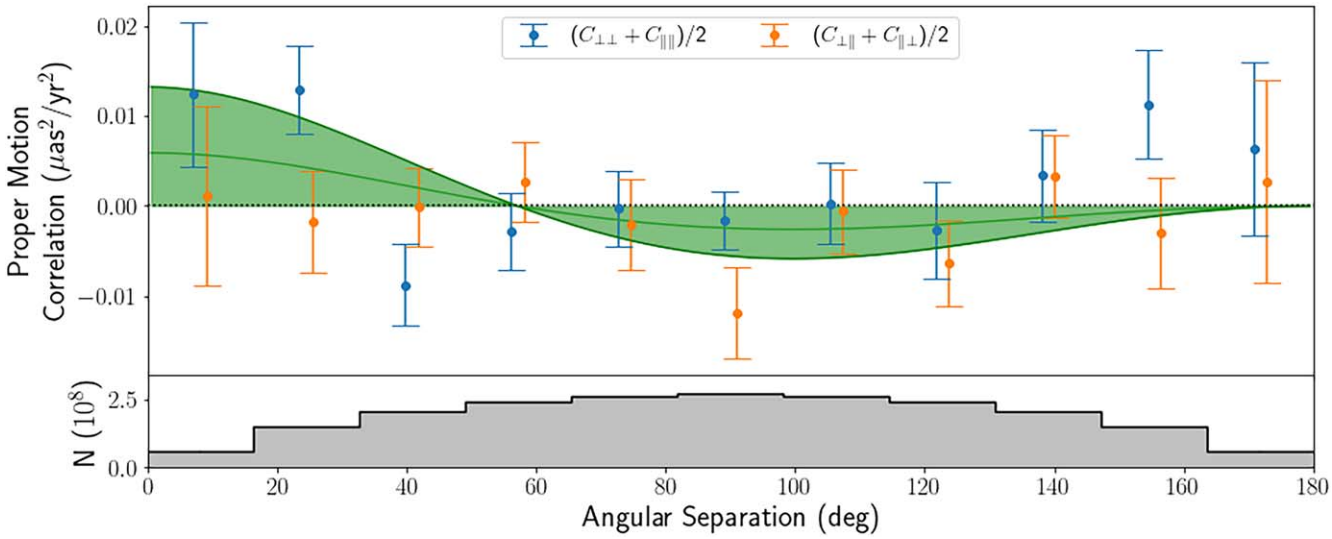

Figure 4. Proper motion power in parallel and perpendicular modes (blue) and mixed modes (orange) vs. the angular separation of quasar pairs for 64,879 quasars selected based on their proper motion amplitude <100 μas yr^{-1}. The points are offset by $\pm1^\circ$ from the center of each angular separation bin for clarity. The green line shows the best-fit (and nonsignificant amplitude) astrometric HD curve to the aligned correlations, $(C_{\perp\perp}+C_{\parallel\parallel})/2$, and the filled region shows the $<95\%$ confidence envelope. This envelope equates to 95% confidence limits on the characteristic strain $h_c \leqslant 2.7\times10^{-12}$ and the gravitational-wave energy density $h_{70}^2\Omega_{\rm GW} \leqslant 0.0096$ at reference frequency $f_{\rm ref}=1$ yr^{-1}. The mixed-mode measurements should be consistent with zero and provide a control on systematics. The lower histogram shows the distribution of quasar pairs, scaled by 10^8.

5. Results

5.1. Vector Spherical Harmonics

Table 1 shows the best-fit VSH dipole and quadrupole coefficients, power, and amplitudes (defined in Appendix). The VSH fits show significant power in the quadrupole with unequal contributions from the E2 and B2 modes, which suggests that there are significant systematic effects in the proper motion vector field. The E2 mode is significant, but the B2 mode is not. If we nonetheless use the total quadrupole power to estimate the energy density in gravitational waves, we obtain $\Omega_{\rm GW}=0.042(0.008)$. This is consistent with the nonsignificant S. Jaraba et al. (2023) value of $h_{70}^2\Omega_{\rm GW}=0.040(0.017)$ for their "intersection" sample of 773,471 quasars with very similar frequency sensitivity. If we assume that the nonsignificant B2 mode is the most constraining and that the significant E2 power is not physical, then we can use the B2 mode as the statistical floor on half of the total power, set both modes to be equal to P_2^t, and obtain the nonsignificant value of $\Omega_{\rm GW}=0.013(0.006)$ or $h_{70}^2\Omega_{\rm GW}\leqslant 0.023$ at 95% confidence, which is nearly identical to VLBI measurements (S. Jaraba et al. 2023). This is a new sensitivity limit for optical astrometry and the first time that it is similar to VLBI. This is also a threefold improvement over recent work using Gaia DR3 quasars.

5.2. Astrometric Hellings–Downs Curve

Figure 4 shows the astrometric HD curve for the aligned and mixed correlations. The best-measured angular scales are roughly between 30° and 150° where the number of pairs is $>2\times10^8$ and the uncertainties are remarkably small, ~0.005 μas^2 yr^{-2}. The uncertainties grow by a factor of 2 for close pairs and antipodal pairs where the number of pairs drops to 6×10^7. There is no significant power in the astrometric correlations, either point by point, in the error-weighted mean power, or based on fitting the HD curve to the aligned correlations data. The scatter in the data is consistent with the uncertainty estimates. The error-weighted mean power in the average of the aligned correlations is 0.0009(0.0015) μas^2 yr^{-2}. The error-weighted mean is $-0.0017(0.0016)$ μas^2 yr^{-2} for the cross terms. The noise-consistent measurements and the consistency between the correlations that should and should not show a gravitational-wave signal demonstrate that we have successfully removed proper motion systematics but have not yet produced an astrometric detection of gravitational waves. There is also little or no evidence of a noise floor: as we grew the sample size, the uncertainties in the HD curve decreased correspondingly and as expected.

A fit of the astrometric HD curve to the aligned correlations, Equations (2) and (3), produces a nonsignificant amplitude: $I_{\rm GW}f^3=0.0029(0.0024)$ μas^2 yr^{-2}. A direct fit to the proper motions does not significantly differ from the fit to the binned data. For a 95% confidence limit of $f^3I_{\rm GW}(f)\leqslant0.0063$ μas^2 yr^{-2}, we obtain a limit on the characteristic strain of

$$h_c \leqslant 2.7\times10^{-12}$$

for $f_{\rm ref}=1$ yr^{-1}. The corresponding limit on the gravitational-wave energy density is

$$h_{70}^2\Omega_{\rm GW}\leqslant 0.0096,$$

also at 95% confidence. This is better than a factor of 2 lower than the VSH measurement corrected for nonequal E- and B-mode quadrupoles and is a factor of 4.4 times lower than the uncorrected quadrupole measurement. This is the strongest astrometric constraint on gravitational waves to date.

6. Discussion and Conclusions

Are these new astrometric limits on strain and energy density constraining on possible sources of the pulsar-timing-based stochastic gravitational-wave background? The characteristic gravitational-wave strain claimed by pulsar timing is $h_c=2.4^{+0.7}_{-0.6}\times10^{-15}$ at a reference frequency of $f_{\rm ref}=1$ yr^{-1},

assuming the strain spectrum appropriate for an ensemble of massive black hole binaries, $h_c(f) \propto f^{-2/3}$ (G. Agazie et al. 2023). This spectral index and strain measurement predict a strain of 2.4×10^{-14} at 1 nHz (1 yr^{-1} is 31.7 nHz), roughly the expected turnover frequency for massive black hole binaries. This is well below the limits obtained from VSH fitting and the astrometric HD curve for quasars, so the astrometry is not constraining on extant observations. It may constrain exotic interpretations of the gravitational-wave background.

This work, however, has produced the first astrometric HD curves and demonstrated a powerful approach to the two transverse dimensions of gravitational-wave detection not probed by pulsar timing. We have also shown how the systematics present in Gaia VSH analysis can be sidestepped and quantified using pairwise angular motions. We have produced the best limits on the stochastic astrometric gravitational-wave background to date, including demonstrating for the first time that optical astrometry can surpass the limits from VLBI, mostly due to sample size.

Future Gaia data releases will improve this measurement, particularly due to longer time baselines (astrometric uncertainties scale roughly as $t^{-3/2}$ if sampling is regular), but the sample size may grow as well. We also expect cross correlations between quasar proper motions and pulsar timing to produce interesting limits or detections. This cross correlation will sample the full three-dimensional realm of observable gravitational-wave effects and can probe the polarization, isotropy, and transverse traceless nature of gravitational waves.

Acknowledgments

We thank A. Williams, D. Hogg, and K. Storey-Fisher for discussion of the Quaia catalog and K. Inomata for helpful discussion of astrometric correlations. We also thank the referee for valuable feedback. This research made use of NumPy (S. van der Walt et al. 2011), Matplotlib (J. D. Hunter 2007), and Astropy,[2] a community-developed core Python package for Astronomy (Astropy Collaboration et al. 2013; A. M. Price-Whelan et al. 2018).

Facilities: Gaia, Sloan.

Software: astropy (Astropy Collaboration et al. 2013; A. M. Price-Whelan et al. 2018), NumPy (S. van der Walt et al. 2011), Matplotlib (J. D. Hunter 2007), `lmfit`(M. Newville et al. 2021), `emcee`(D. Foreman-Mackey et al. 2013), TOPCAT (M. B. Taylor 2005).

Appendix
Dipole and Quadrupole Vector Spherical Harmonics

The VSH modes that are fit to vector fields are obtained from the divergence and curl of the scalar spherical harmonics $Y_{\ell m}$:

$$\boldsymbol{S}_{\ell m}(\alpha, \delta) = \frac{1}{\sqrt{\ell(\ell+1)}} \boldsymbol{\nabla} Y_{\ell m}(\alpha, \delta) \tag{A1}$$

and

$$\boldsymbol{T}_{\ell m}(\alpha, \delta) = \frac{-1}{\sqrt{\ell(\ell+1)}} \hat{n} \times \boldsymbol{\nabla} Y_{\ell m}(\alpha, \delta), \tag{A2}$$

where the $\boldsymbol{S}_{\ell m}$ is the "spheroidal" curl-free E mode of degree ℓ and order m, $\boldsymbol{T}_{\ell m}$ is the "toroidal" divergenceless B mode, and $\hat{n}$ is the radial unit vector (F. Mignard & S. Klioner 2012). The E modes, B modes, and radial vector $\hat{n}$ are mutually orthogonal by construction. A general vector field on a sphere can be fully described by a sum of these VSH with complex spheroidal and toroidal coefficients $s_{\ell m}$ and $t_{\ell m}$:

$$\boldsymbol{V}(\alpha, \delta) = \sum_{\ell=1}^{\infty} \sum_{m=-\ell}^{\ell} (s_{\ell m} \boldsymbol{S}_{\ell m}(\alpha, \delta) + t_{\ell m} \boldsymbol{T}_{\ell m}(\alpha, \delta)). \tag{A3}$$

The decomposition of a real vector field into VSH always produces real-valued solutions.

Following the formalism of F. Mignard & S. Klioner (2012), the dipole vector fields $\boldsymbol{V}_{E1}$ and $\boldsymbol{V}_{B1}$ have the form

$$\begin{aligned} \boldsymbol{V}_{E1}(\alpha, \delta) = & \frac{1}{2}\sqrt{\frac{3}{\pi}} (s_{11}^{Re} \sin\alpha + s_{11}^{Im} \cos\alpha)\hat{\boldsymbol{e}}_\alpha \\ & + \frac{1}{2}\sqrt{\frac{3}{\pi}} \left(s_{10} \sqrt{\frac{1}{2}} \cos\delta \right. \\ & \left. + s_{11}^{Re} \cos\alpha \sin\delta - s_{11}^{Im} \sin\alpha \sin\delta \right) \hat{\boldsymbol{e}}_\delta \end{aligned} \tag{A4}$$

$$\begin{aligned} \boldsymbol{V}_{B1}(\alpha, \delta) = & \frac{1}{2}\sqrt{\frac{3}{\pi}} \left(t_{10} \sqrt{\frac{1}{2}} \cos\delta \right. \\ & \left. + t_{11}^{Re} \cos\alpha \sin\delta - t_{11}^{Im} \sin\alpha \sin\delta \right) \hat{\boldsymbol{e}}_\alpha \\ & + \frac{1}{2}\sqrt{\frac{3}{\pi}} (-t_{11}^{Re} \sin\alpha - t_{11}^{Im} \cos\alpha) \hat{\boldsymbol{e}}_\delta, \end{aligned} \tag{A5}$$

where $\hat{\boldsymbol{e}}_\alpha$ and $\hat{\boldsymbol{e}}_\delta$ are the unit vectors in the R.A. and decl. directions, respectively. The superscripts *Re* and *Im* indicate the real or imaginary parts of the coefficients (the $m = 0$ coefficients are always real).

The maximum dipole proper motion, which we call its amplitude, is calculated via

$$A_{\mathrm{E1,B1}} = \frac{\sqrt{P_\ell^{s,t}}}{2\sqrt{2\pi/3}}, \tag{A6}$$

and the dipole apex directions $\alpha^*_{\mathrm{E1,B1}}$ and $\delta^*_{\mathrm{E1,B1}}$ are

$$\tan\alpha^*_{\mathrm{E1}} = \frac{-s_{11}^{Im}}{s_{11}^{Re}} \tag{A7}$$

$$\tan\delta^*_{\mathrm{E1}} = \frac{-s_{10}}{\sqrt{2}\,(s_{11}^{Re}\cos\alpha^*_{\mathrm{E1}} - s_{11}^{Im}\sin\alpha^*_{\mathrm{E1}})} \tag{A8}$$

$$\tan\alpha^*_{\mathrm{B1}} = \frac{-t_{11}^{Im}}{t_{11}^{Re}} \tag{A9}$$

$$\tan\delta^*_{\mathrm{B1}} = \frac{-t_{10}}{\sqrt{2}\,(t_{11}^{Re}\cos\alpha^*_{\mathrm{B1}} - t_{11}^{Im}\sin\alpha^*_{\mathrm{B1}})}. \tag{A10}$$

[2] http://www.astropy.org

The quadrupole vector fields are

$$\begin{aligned}\boldsymbol{V}_{E2}(\alpha,\,\delta) = \frac{1}{2}\sqrt{\frac{5}{\pi}}\,(s_{21}^{Re}\,\sin\alpha\sin\delta + s_{21}^{Im}\,\cos\alpha\sin\delta \\ -s_{22}^{Re}\,\sin 2\alpha\cos\delta - s_{22}^{Im}\,\cos 2\alpha\cos\delta)\hat{\boldsymbol{e}}_{\alpha} \\ + \frac{1}{2}\sqrt{\frac{5}{\pi}}\left(s_{20}\,\frac{1}{2}\sqrt{\frac{3}{2}}\,\sin 2\delta - s_{21}^{Re}\,\cos\alpha\cos 2\delta\right. \\ + s_{21}^{Im}\,\sin\alpha\cos 2\delta - s_{22}^{Re}\,\frac{1}{2}\cos 2\alpha\sin 2\delta \\ \left. + s_{22}^{Im}\,\frac{1}{2}\,\sin 2\alpha\sin 2\delta\right)\hat{\boldsymbol{e}}_{\delta} \qquad \text{(A11)}\end{aligned}$$

$$\begin{aligned}\boldsymbol{V}_{B2}(\alpha,\,\delta) = \frac{1}{2}\sqrt{\frac{5}{\pi}}\left(t_{20}\,\frac{1}{2}\sqrt{\frac{3}{2}}\,\sin 2\delta\right. \\ - t_{21}^{Re}\,\cos\alpha\cos 2\delta + t_{21}^{Im}\,\sin\alpha\cos 2\delta \\ - t_{22}^{Re}\,\frac{1}{2}\,\cos 2\alpha\sin 2\delta \\ \left. + t_{22}^{Im}\,\frac{1}{2}\,\sin 2\alpha\sin 2\delta\right)\hat{\boldsymbol{e}}_{\alpha} \\ + \frac{1}{2}\sqrt{\frac{5}{\pi}}\,(-t_{21}^{Re}\,\sin\alpha\sin\delta \\ - t_{21}^{Im}\,\cos\alpha\sin\delta + t_{22}^{Re}\,\sin 2\alpha\cos\delta \\ + t_{22}^{Im}\,\cos 2\alpha\cos\delta)\hat{\boldsymbol{e}}_{\delta}. \qquad \text{(A12)}\end{aligned}$$

The power in mode ℓ is obtained from the quadrature sum of coefficients (modulo factors of 2):

$$P_{\ell} = s_{\ell 0}^2 + t_{\ell 0}^2 + 2\sum_{m=1}^{\ell}\left[(s_{\ell m}^{Re})^2 + (s_{\ell m}^{Im})^2 + (t_{\ell m}^{Re})^2 + (t_{\ell m}^{Im})^2\right] \qquad \text{(A13)}$$

(F. Mignard & S. Klioner 2012). To compute the power in Eℓ or Bℓ modes separately, simply omit the $t_{\ell m}$ or $s_{\ell m}$ terms in the sum.

ORCID iDs

Jeremy Darling https://orcid.org/0000-0003-2511-2060

References

Abbott, B. P., Abbott, R., Abbott, T. D., et al. 2016, PhRvL, 116, 061102
Afzal, A., Agazie, G., Anumarlapudi, A., et al. 2023, ApJL, 951, L11
Agazie, G., Anumarlapudi, A., Archibald, A. M., et al. 2023, ApJL, 951, L8
Astropy Collaboration, Robitaille, T. P., Tollerud, E. J., et al. 2013, A&A, 558, A33
Book, L. G., & Flanagan, E. E. 2011, PhRvD, 83, 024024
Çalışkan, M., Chen, Y., Dai, L., et al. 2024, JCAP, 2024, 030
Chen, S., Sesana, A., & Del Pozzo, W. 2017, MNRAS, 470, 1738
Darling, J. 2012, ApJL, 761, L26
Darling, J., Truebenbach, A. E., & Paine, J. 2018, ApJ, 861, 113
Enoki, M., & Nagashima, M. 2007, PThPh, 117, 241
Foreman-Mackey, D., Hogg, D. W., Lang, D., & Goodman, J. 2013, PASP, 125, 306
Gaia Collaboration, Bailer-Jones, C. A. L., Teyssier, D., et al. 2023, A&A, 674, A41
Gaia Collaboration, Klioner, S. A., Lindegren, L., et al. 2022, A&A, 667, A148
Gaia Collaboration, Klioner, S. A., Mignard, F., et al. 2021, A&A, 649, A9
Gaia Collaboration, Prusti, T., de Bruijne, J., H., J., et al. 2016, A&A, 595, A1
Golat, S., & Contaldi, C. R. 2022, PhRvD, 105, 063502
Gwinn, C. R., Eubanks, T. M., Pyne, T., Birkinshaw, M., & Matsakis, D. N. 1997, ApJ, 485, 87
Hellings, R. W., & Downs, G. S. 1983, ApJL, 265, L39
Hunter, J. D. 2007, CSE, 9, 90
Inomata, K., Kamionkowski, M., Toral, C. M., & Taylor, S. R. 2024, PhRvD, 110, 063547
Jaraba, S., García-Bellido, J., Kuroyanagi, S., Ferraiuolo, S., & Braglia, M. 2023, MNRAS, 524, 3609
Kelley, L. Z., Blecha, L., Hernquist, L., Sesana, A., & Taylor, S. R. 2017, MNRAS, 471, 4508
Lindegren, L., Klioner, S. A., Hernández, J., et al. 2021, A&A, 649, A2
Mignard, F., & Klioner, S. 2012, A&A, 547, A59
Mihaylov, D. P., Moore, C. J., Gair, J. R., Lasenby, A., & Gilmore, G. 2018, PhRvD, 97, 124058
Moore, C. J., Cole, R. H., & Berry, C. P. L. 2015, CQGra, 32, 015014
Moresco, M., Amati, L., Amendola, L., et al. 2022, LRR, 25, 6
Newville, M., Otten, R., Nelson, A., et al. 2021, lmfit/lmfit-py, v1.0.3, Zenodo, doi: 10.5281/zenodo.5570790
O'Beirne, L., & Cornish, N. J. 2018, PhRvD, 98, 024020
Price-Whelan, A. M., Sipőcz, B. M., Günther, H. M., et al. 2018, AJ, 156, 123
Pyne, T., Gwinn, C. R., Birkinshaw, M., Eubanks, T. M., & Matsakis, D. N. 1996, ApJ, 465, 566
Qin, W., Boddy, K. K., Kamionkowski, M., & Dai, L. 2019, PhRvD, 99, 063002
Sesana, A., Haardt, F., Madau, P., & Volonteri, M. 2004, ApJ, 611, 623
Storey-Fisher, K., Hogg, D. W., Rix, H.-W., et al. 2024, ApJ, 964, 69
Taylor, M. B. 2005, in ASP Conf. Ser. 347, Astronomical Data Analysis Software and Systems XIV, ed. P. Shopbell, M. Britton, & R. Ebert (San Francisco, CA: ASP), 29
Titov, O., Lambert, S. B., & Gontier, A. M. 2011, A&A, 529, A91
Truebenbach, A. E., & Darling, J. 2017, ApJS, 233, 3
van der Walt, S., Colbert, S. C., & Varoquaux, G. 2011, CSE, 13, 22